Theranostic carbon dots with innovative NIR-II emission for *in vivo* renal excreted optical imaging and photothermal therapy

Youbin Li,[†] *Gongxun Bai,*[‡] *Songjun Zeng*[†]**, Jianhua Hao*[‡]***

[†]Synergetic Innovation Center for Quantum Effects and Application, Key Laboratory of Low-dimensional Quantum Structures and Quantum Control of Ministry of Education, School of Physics and Electronics, Hunan Normal University, Changsha, 410081, P.R. China.

[‡]Department of Applied Physics, The Hong Kong Polytechnic University, Hong Kong (China)

KEYWORDS: carbon dots, NIR-triggered NIR-II emission, renal clearance, photothermal therapy of cancer, Diagnosis and treatment integration CDs

ABSTRACT: Carbon dots (CDs) with low biotoxicity, high photostability, and well-controlled small size are highly desirable imaging agents for optical bioimaging. However, most of the CDs triggered by ultraviolet (UV)/blue light present visible/first near infrared (NIR-I) emissions shorter than 820 nm, impairing their imaging applications *in vivo* by low penetration depth. Hence, developing novel CDs based materials with second near infrared (NIR-II) emission located in 1000-1700 nm region is an urgent task. Here, a novel NIR-II emitting CDs-based nanoprobe triggered by 808 nm laser is developed. The designed CDs with 900-1200 nm luminescence possess high quantum yield (QY-0.4%), and high biocompatibility, which have proven to be effective probes for *in vivo* NIR-II bioimaging. Notably, nearly 65% CDs are excreted from mouse urine within 6 h, further demonstrating the rapid renal clearance of CDs. Furthermore, the designed CDs also exhibit high photothermal efficiency (30.6%), making them ideal materials for thermal ablation of cancer. Our findings pave the way of designing multifunctional CDs-based theranostic platform for simultaneously integrating the advanced NIR-II bioimaging and photothermal therapy (PTT) of cancer.

Carbon nanomaterials recently have garnered extensive interest for various applications in fluorescence ink[1,2], optoelectronic devices[3,4], and bioimaging field[5-10]. Taking advantages of their unique optical properties, including the high biocompatibility, high quantum yield (QY), tunable fluorescence properties, and small size, CDs have emerged as promising nanomaterials for biomedical applications[5-20]. However, most of the CDs triggered by UV/blue light present visible/first near infrared (NIR-I) emissions shorter than 820 nm[21-23], remarkably hindering their *in vivo* applications. In comparison with visible/NIR-I light-based bioimaging, fluorescence imaging in NIR-II region (1000-1700 nm) presents significantly reduced scattering losses, enabling the observation of processes deeper in living animals and higher spatial resolution[24-35]. Therefore, exploring NIR-triggered CDs with NIR-II emission is significant importantce, making them more competitive for further biomedical applications.

To date, attempts of developing CDs with efficient emissions in the visible and NIR region have been reported[5-20]. Sun and co-workers first developed the blue light emissive CDs for biological imaging under the excitation of UV light[18]. Recently, Yang and co-workers[8] reported a red-emissive CDs with primary emissions at 650 and 710 nm. Zhang and co-workers[21] showed the 731/820 nm emission CDs with relative low photoluminescence (PL) QY of 0.2% and inefficient excitation of 526 nm laser by doping S/Se. Very recently, Qu and co-workers[9] have proposed a NIR-II laser triggered two photon NIR emission (~732 nm) of CDs. However, two photon induced NIR emission was only achieved under the excitation of an expensive and complex femtosecond pulse laser. Up to now, CDs capable of emitting NIR-II signal triggered by conventional NIR light source have not yet been explored, which still remained a great challenge. Hence, developing a facile strategy to design NIR-II emissive CDs with high QY, good biocompatibility under the excitation in the NIR window is highly imperative.

Herein, watermelon-derived CDs with NIR-II emission were explored for the first time as *in vivo* optical fluorescence agent. The CDs with high QY, high photostability and rapid renal clearance are desirable contrast agents for fluorescence bioimaging. NIR-II bioimaging based on the designed CDs was successfully demonstrated. Apart from the excellent optical nature, the CDs also exhibit excellent 808 nm laser inducible photothermal properties for PTT of cancer.

RESULTS AND DISCUSSION

Scheme 1 presents a facile method for synthesis of CDs with efficient NIR-II emission under 808 nm excitation by using watermelon juice as carbon source was demonstrated. As presented in the transmission electron microscopy (TEM) image (**Figure 1a**), the CDs holded highly uniform sphere-like structure with size of about 6 nm. And dynamic light scattering (DLS) measurement (**Supplementary Figure S1)** demonstrated that the size was also distributed between 4-12 nm, matching well with TEM results. Moreover, the surface charge of CDs was also investigated by zeta potential analysis, indicating the negative charge nature on the surface (-4.9 mV, **Supplementary Figure S2**). The interplanar distance of 0.21 nm was estimated from the inset of Figure 1a, which was consistent with (100) crystal plane of CDs. To further prove the crystal phase of CDs, powder X-ray diffraction (XRD) was performed (Figure 1b). As demonstrated, a broad peak corresponding to (002) crystal plane located at 21 º was observed, which was similar to the previous reports.[2,10] The element compositions in CDs were also revealed by using the X-ray photoelectron spectroscopy (XPS, Figure 1c and **Table S1**). The compositions of C (81.24%), N (4.9%), and O (14.9%) in the CDs were successfully determined. The magnified C 1s spectrum (Figure 1d) of CDs presents obvious C=C/C-C (284.3 eV), C-O/C-N (285 eV), and C=O (286.3 eV) peaks. In addition, the contents of the different typed chemical bonds in CDs were shown in **Table S2**. Fourier transform infrared (FTIR, **Supplementary**

Figure S3) spectra were further used for evaluating the surface ligands. As demonstrated, the stretching vibrations related to C-OH, C-H are observed at 3430, and 2923/2856 cm^{-1}, respectively. The characterization absorption peak at 1630 cm^{-1} can be ascribed to the C=O vibrating. In addition, as demonstrated in Raman spectra (**Supplementary Figure S4),** the D and G bands at 1350 cm^{-1} and 1598 cm^{-1} can not be identified, due to bright fluorescence emission of CDs[2].

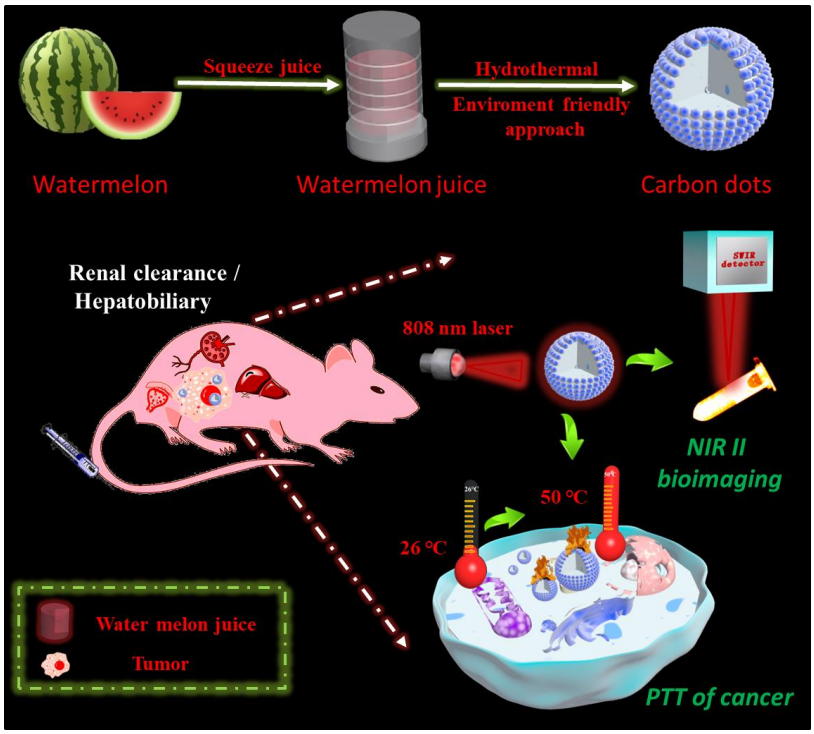

Scheme 1. Schematic illustration of the synthesis of the NIR-II emitting CDs for rapid renal clearance NIR-II bioimaging and PTT therapy of cancer.

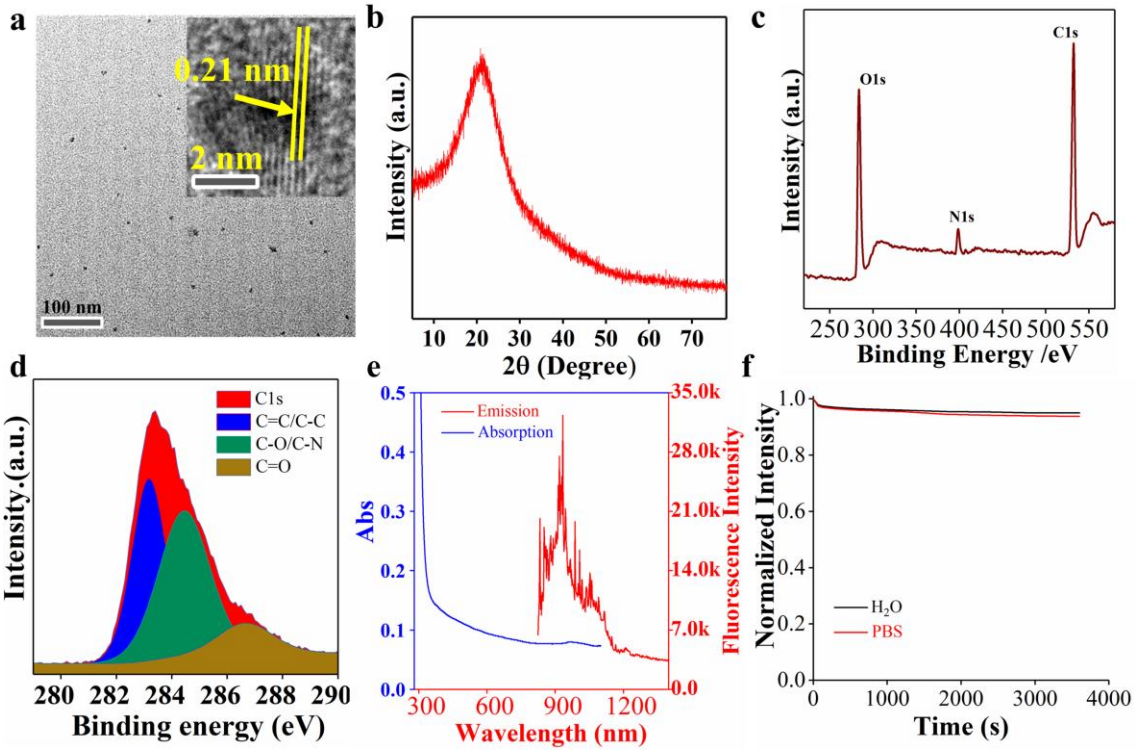

Figure 1. (a) TEM and high resolution TEM image of CDs. (b) XRD pattern of the as prepared CDs. (c) XPS survey spectrum of the CDs. (d) the high resolution of C1s XPS. (e) the UV-Vis absorption and fluorescent emission spectrum (808 nm excitation) of CDs. (f) Photostability curves of CDs in water and PBS under 808 nm laser irradiation for 1h (1 W cm^{-2}).

To reveal the NIR absorption/emission properties, the UV-Vis and NIR-II emission spectrum of CDs in water was analyzed. UV-Vis result (Figure 1e) exhibits a broad-band absorption in 400-800 nm. And under the 808 nm laser excitation, the designed CDs presented an obvious NIR-II emission from 900-1200 nm with peak centered at 925 nm (Figure 1e). The quantum yield (QY) of CDs in water was further measured to be about 0.4% by utilizing the IR-26 dye as reference[36]. Our measurement exhibited higher QY than the explored CH1055 dye (QY=0.3%)[36], implying that the synthesized CDs are more promising probes for NIR-II bioimaging[36]. One of key features for the usefulness of the nanoprobes in bioimaging application is the photo-stability of the nanoparticles in water. Therefore, the photo-stabilities (Figure 1f) of

CDs in water and phosphate-buffered saline (PBS) were measured using 808 nm laser irradiation. As illustrated in Figure 1f and **Supplementary Figure S5**, both of the CDs solutions in water and PBS exhibit high photo-stability with lower photobleaching degree < 5% than the previously reported molecular NIR-II probe (about 10%)[20]. It is noted that the NIR-II emissive CDs with high photostability are beneficial for *in vivo* NIR-II optical bioimaging.

The excitation-dependent fluorescence emitting behavior of CDs was further analyzed. As presented in **Supplementary Figure S6**, by adjusting the excitation light from 250 to 400 nm, the tunable fluorescence emission wavelengths were detected from 400 to 474 nm, which was similar with the previously reported CDs[37,38]. However, it should be pointed out that apart from the visible emission, the CDs also present NIR-II emission under 808 nm excitation, which has not been observed in the previous report by using the traditional Si-based detector. To further reveal the NIR-II emission of the CDs, *in vitro* phantom imaging (**Supplementary Figure S7)** of the watermelon juice was first performed. As demonstrated, almost no fluorescent signal was observed, unambiguously indicating the NIR-II emission was originated from the synthesized CDs. Moreover, the element compositions of the as-prepared CDs were further conformed via inductively coupled plasma mass spectrometry (ICP-MS, **Table S3**), demonstrating the absence of other impurities of NIR-II emitter ions. These findings verify that the NIR-II emission is originated from the designed CDs.

To reveal the emission property of CDs achieved by using other raw material, the lemon juice was also used for preparing CDs. As presented in **Supplementary Figure S8**, TEM result revealed that the lemon juice-based CDs also presented highly uniform sphere-like structure. *In vitro* phantom images (**Supplementary Figure S9)** of the watermelon juice-based and lemon juice-based CDs demonstrated that the watermelon juice-based CDs holded brighter NIR-II

emission, making it more competitive for NIR-II optical-guided bioimaging. Aforementioned FTIR results demonstrated the existence of abundant oxygen groups, including the hydroxyl (3428 cm^{-1}) and carbonyl (1630 cm^{-1}) groups. It is noted that surface oxidation triggered defect state can serve as capturing centers for excitons, subsequently leading to fluorescence emission[39,40]. Therefore, on the basis of the surface oxidation induced surface states, we speculate that the NIR-II emission of CDs is mainly attributed to the higher degree of surface oxidation. However, the NIR-II emitting mechanism of the designed CDs is still needed for further study.

Before bioimaging applications, cytotoxicity of CDs in bronchial epithelial normal and HeLa cells was first tested via the 3-(4,5-dimethylthiazol-2-yl)-2,5 diphenyl-tetrazolium bromide (MTT) assay. And, the cell viabilities (**Supplementary Figure S10 and S11)** of CDs in HeLa and bronchial epithelial normal cells treated with CDs are all exceeded 95%, revealing the low cytotoxicity of CDs. Based on the above features of CDs, we moved forward to perform *in vivo* bioimaging using a NIR-II imaging apparatus[41,42] with a 1000-1400 nm band pass filter. As demonstrated in **Figure 2a**, within 1 min injection, an intense NIR-II emitting signal was appeared in mouse kidney. With time elapse, the signal was strengthed at 0.5 h post injection and decreased after 1 h injection. After 6 h injection, the optical signal in kidney was tended to very weak, revealing the rapid excretion of CDs from the mouse by renal clearance. While, in supine positioned mouse, as shown in Figure 2a, strong fluorescence signals in bladder and relative weak signals in liver were observed, further revealing the primary renal excretion of CDs.

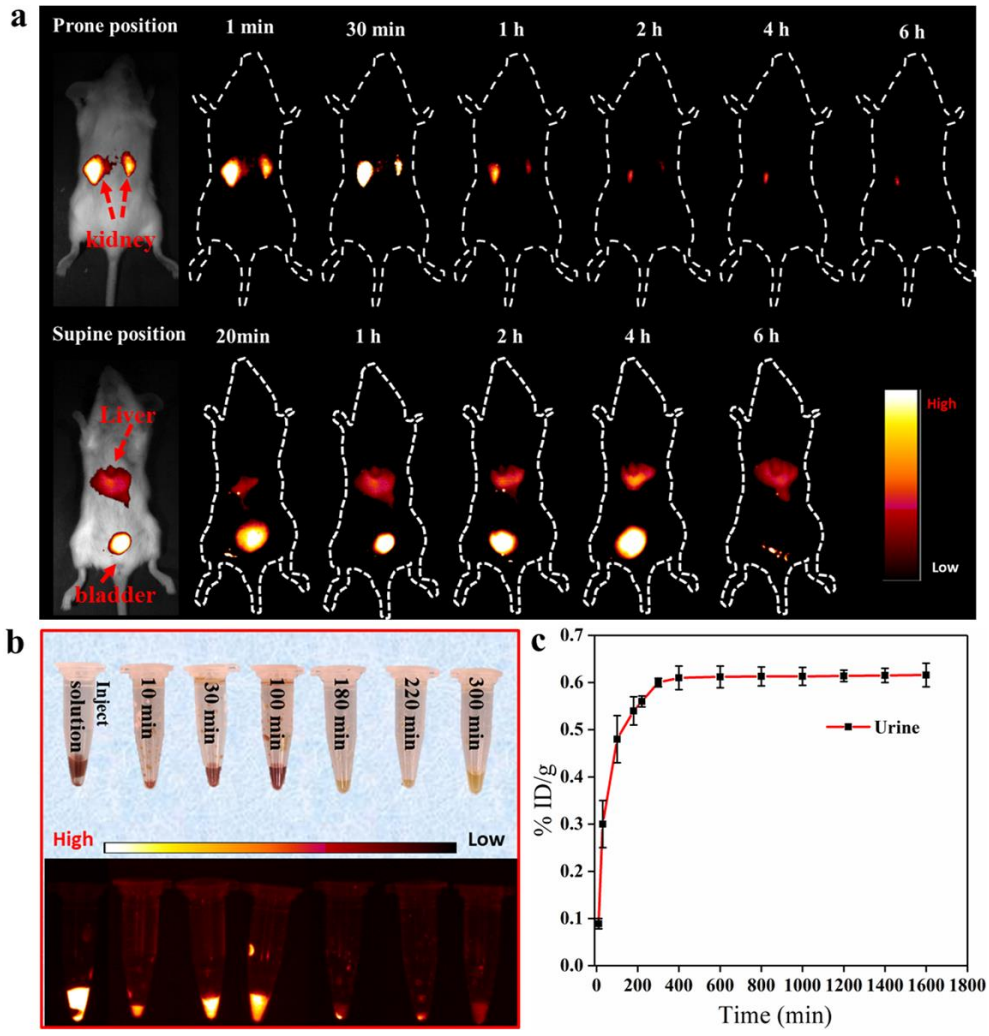

Figure 2. (a) Time-dependent bioimaging of mouse treated with CDs (20 μg/g) through tail vein. (b) The digital camera photographs and corresponding *in vitro* phantom imaging of the urine samples collected at different period time after intravenously injected with CDs solution. (c) CDs cumulative urine excretion curve.

Moreover, the fluorescence signal in the liver was enhanced with prolonging time. The fluorescence signal in the liver showed maximum value after 24 h injection (**Supplementary Figure S12**) and tended to be decreased after 48 h injection. Subsequently, the NIR-II optical signal in the liver was scarcely observed after 7 days injection, revealing the excretion of CDs *in vivo via* hepatobiliary route. In addition, the maximum signal intensity (**Supplementary Figure**

S13) in bladder showed about 1.5 times higher than that in liver, revealing the main renal clearance pathway of CDs. For further demonstrating excretion mechanism, the dissected organs (including the heart, liver, spleen, lung, kidney) are imaged to obtain the accurate biodistribution of CDs by using the same system. As shown in **Supplementary Figure S14 and S15,** remarkable fluorescence signals in liver and kidney were observed. A new weak fluorescence in spleen is observed at 0.5 h post-injection and disappeared after 12 h injection. The bioimaging results reveal the main renal excretion of CDs from the body, owing to the fast decreased fluorescence intensity in renal. Thus, the designed CDs in smaller size (<6 nm) exhibit advantage of rapid renal excretion from mice, which avoids the problem of unintended nonspecific organ uptake and long retention time in reticuloendothelial system.[43]

To further elucidate the excretion kinetics of CDs in the living body, the urine from mouse intravenous injection with CDs was collected over 24 h. As revealed in Figure 2b, *in vitro* phantom imaging of mouse urines showed a decreased fluorescence signal with the extension of time. And, the urine was visibly dark brown owing to the existence of CDs, and gradually turned to yellowish as a function of time, further verifying the rapid renal excretion of CDs from the urine. Moreover, the TEM image (**Supplementary Figure S16**) of the urine gathered after 2 h injection exhibited the same particle shape with the CDs, undoubtedly revealing the existence of CDs in the urine and the negligible size change of CDs after renal excretion from the living mouse. The renal clearance of CDs from the mouse was further calculated by measuring the concentration of CDs in the urine based on the emission intensity[36]. From the urine excretion data (Figure 2c), 65% of the CDs were cleared from urine after 6 h post injection, revealing the main renal clearance of CDs and slightly hepatobiliary excretion (35%). These results reveal that

the CDs with efficient NIR-II emission under 808 nm excitation and main renal excretion are desirable probes for bioimaging applications.

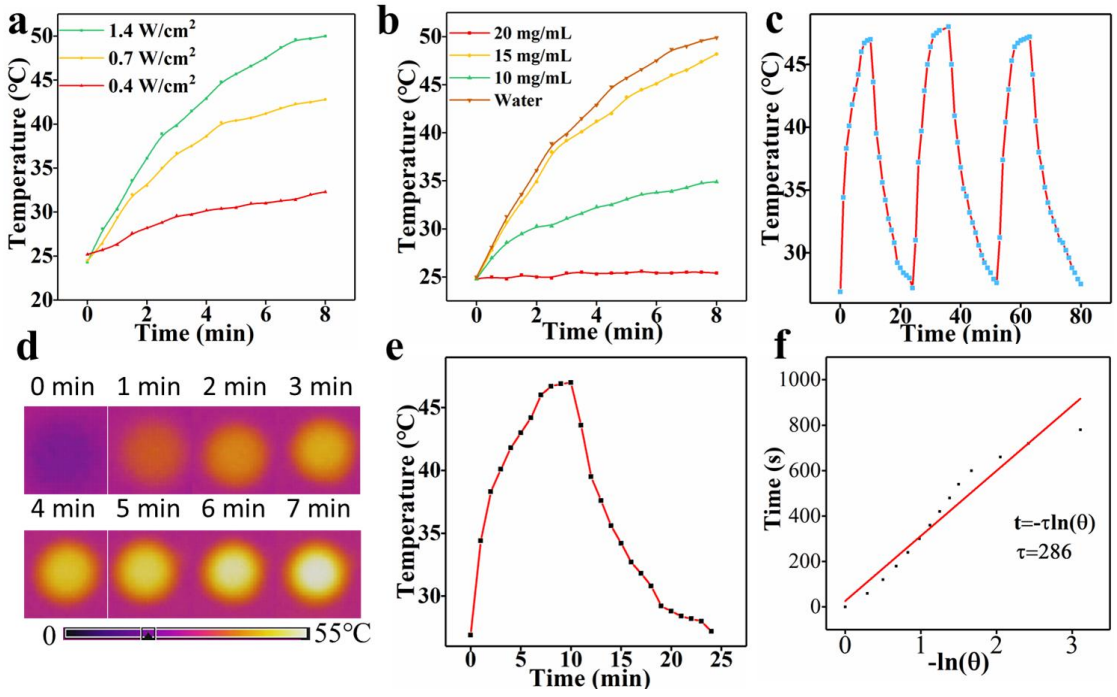

Figure 3. (a) Temperature curves of CDs solution (20 mg/mL) recorded with 808 nm laser irradiation. (b) Temperature curves of different concentrations of CDs solutions under 808 nm laser irradiation (1.4 W cm^{-2}). (c) The photothermal profiles of CDs solution (15 mg/mL) with three irradiation cycles with exposure to 808 nm laser (1.4 W cm^{-2}). (d) Thermal infrared images of the CDs solutions (15 mg/mL) recorded after 808 nm laser irradiation for 7 min (1.4 W cm^{-2}). (e) Heating and cooling curves of CDs aqueous solution (15 mg/mL) measured with irradiation of 808 nm laser (1.4 W cm^{-2}). (f) The linear time data and –lnθ acquired from cooling period of Figure 3e. The time constant for heat transfer of the CDs was calculated to be 286 s.

Apart from the excellent NIR-II emission, owing to the NIR absorption, the CDs can be utilized as promising photothermal agent[44-48]. Then, *in vitro* photothermal conversion properties

of CDs were studied. The temperature change curve of CDs solution was detected under the irradiation of 808 nm laser. As shown in **Figure 3a**, the temperature of CDs solution under high power density irradiation (1.4 W cm^{-2}) for 8 min was increased by 25 ℃. In addition, the CDs solutions with different concentrations were irradiated with 808 nm laser (1.4 W cm^{-2}). The concentration-dependent temperature curves (Figure 3b) were achieved. And CDs solution with concentration of 20 mg/mL presents rapid temperature increase up to 50 ℃, in contrast, the temperature of the pure water almost remained unchanged. To further evaluate the photothermal stability of CDs solution, the CDs solution was first irradiated with 808 nm laser until the solution reached a steady temperature, and then cooled to room temperature. After 3 cycles of laser off/on (Figure 3c), the temperature elevation showed little difference, proving the high photothermal stability of CDs solution. In addition, the infrared thermal images of CDs solution (Figure 3d) were collected and photothermal conversion efficiency was evaluated to be 30.6% based on the obtained data (Figure 3e and 3f) in the similar way to previous report[10].

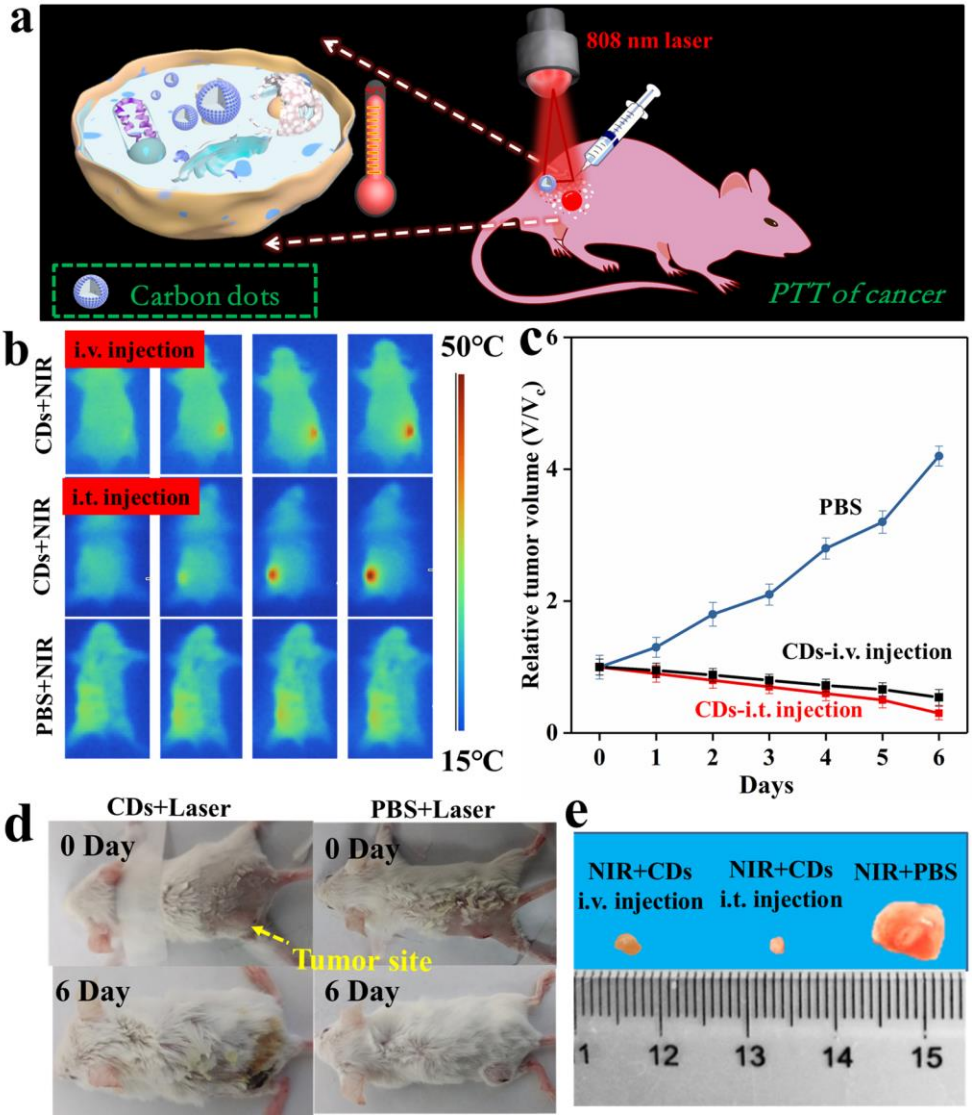

Figure 4. (a) Schematic diagram of PTT therapy of cancer *in vivo*. (b) Representative infrared thermal images of tumor-bearing mice with intravenous (i.v.) injection, intratumoral (i.t.) injection of CDs (50 μL, 20 mg/mL) and PBS (50 μL) into the tumor site under 808 nm laser irradiation. (c) Time course change in the relative volume after treatment by using CDs and PBS (n=5 per group). (d) Digital photographs of the tumor-bearing mice after different treatments. (e) Photographs of tumors harvested from mice in 6 days after different treatments.

Prior to *in vivo* PTT, *in vitro* photothermal ablation (**Supplementary Figure S17)** of HeLa cells incubated with different contents of CDs was studied. As demonstrated, without irradiation

by 808 nm laser, even treated with 20 mg/mL of CDs, the viability is still higher than 80%, revealing that the excellent biocompatibility of CDs. While, the cell viability was significantly decreased to less than 10% with exposure to 808 nm laser, indicating the efficient *in vitro* photothermal ablation of cancer cells, implying the promising PTT of cancer. For the study of PTT therapeutic effect of CDs, *in vivo* PTT effects were assessed. Three groups of mice were used: the mice in the control group were intratumorally injected with PBS solution in the tumor site (group I), the experiment group mice were intratumorally injected with CDs solution (group II), the third experiment group mice were intravenously injected with CDs solution (group III). The infrared thermal images of groups II and III (Figure 4a and 4b) showed a rapid temperature increment from 28 ℃ to 50 ℃ within 6 min, whereas there was only 5 ℃ temperature increase in the group I, proving the efficient *in vivo* PTT effect of CDs. To monitor CDs-based PTT efficacy, the tumor-bearing mice were irradiated by a 808 nm laser for 10 min every day. The tumor's volume and the corresponding digital pictures of the mice were recorded (Figure 4c and 4d). After 6 days treatment, the tumor in the groups II and III was almost disappeared (Figure 4d and 4e) when compared with the group I. These findings reveal the potential application of CDs for PTT therapy of cancer.

Histological assessment was further performed to assess the biotoxicity of CDs *in vivo*. As shown in **Supplementary Figure S18**, the major tissues were dissected from the untreated control mouse and test mice after intravenously injected with CDs for 5 and 10 days, respectively. No detectable damage could be observed, proving the high biocompatibility and absence of side effects of CDs.

In conclusion, a new type of theranostic CDs-based probe integrating the new advanced NIR-II imaging and PTT was explored for the first time by an environmentally friendly

hydrothermal method using watermelon juice as a carbon source. By combining ultrasmall particle size, efficient NIR absorption/emission and good biocompatibility, renal clearable NIR-II bioimaging was demonstrated based on the CDs. Interestingly, except for the excellent optical properties, the NIR-II-emitting CDs also exhibit high photothermal efficiency, which can be used for PTT of tumor. The designed CDs with efficient NIR-II emission (QY-0.4%) and high photothermal conversion efficiency (30.6%) break the limitation of *in vivo* high sensitive optical imaging unattained by using the traditional visible light emitting CDs, making the CDs more competitive in optical imaging field.

METHODS

Synthesis of CDs. For the synthesis of water soluble CDs, 20 mL of watermelon juice was added into a Teflon-lined autoclave. After reaction at 190 ℃ for 3 h, the solution was cooled down to 20 ℃. Then the product was first centrifugated at 5000 rpm and the final CDs were obtained from the remanent supernatant solution via further centrifugation.

Chemical and optical characterizations of CDs. XRD analysis was carried out on a Rigaku D/max 2500 system with Cu-Kα radiation. The shape and structure of CDs were assessed by TEM (FEI Tecnai F20). The NIR-II emission spectra of CDs were recorded on a NIRQuest512 spectroscopy. The UV-Vis absorption spectrum was collected by using a UV-1800 spectrophotometer. XPS was tested by a Escalab 250Xi spectrometer. DLS and zeta potential tests of CDs were carried out on a Zetasizer Nano ZS system. The Raman spectrum was recorded on a Raman spectrometer (Renishaw model 1000). The surface ligands of the CDs were investigated by using a FTIR spectrometer (Magna 760, Nicolet).

Cytotoxicity Assay. A typical MTT proliferation assay method was used to assess the *in vitro* cytotoxicity of CDs in bronchial epithelial normal and HeLa cells[41]. Cells were placed into a 96-well microplate filled with 10% fetal bovine serum, 1% penicillin and kept at 37 ℃ with 5% CO_2.[41] Then the CDs with different concentrations (0, 100, 200, 500, 1000, μg/mL) was added into each well for 24 h incubation. Then, the cell viability was evaluated via MTT method.

***In vitro* photothermal ablation.** HeLa cells were used for the *in vitro* photothermal ablation test. HeLa cells were cultured in a 96-well microplate. Then CDs with different concentrations (0, 100, 200, 500, 1000, 2000, 4000, 8000, 15000 and 20000 μg/mL) were added and incubated for 24 h. Then, the cells were treated with 808 nm laser for 10 min, the cell viability was measured by the MTT method as described above.

NIR-II fluorescence bioimaging. *In vivo* NIR-II bioimaging was performed on an animal optical imaging system installed with an InGaAs camera (NIRvanaTM) and a fiber-coupled 808 nm laser [41,42]. The mouse was first anesthetized by pentobarbital sodium solution, subsequently, 150 μL of CDs (20 μg/g) solution was administrated through tail vein. The NIR-II imaging picture was taken on the *in vivo* bioimaging system under 808 nm laser excitation (50 mW cm^{-2}) through a band pass filter (1000-1400 nm). *Ex vivo* NIR-II imaging was also demonstrated by using the imaging system under identical conditions. The animals used in the experiment were complied with the institutional animal use of Hunan Normal University approved by the Laboratory Animal Center of Hunan Province.[41]

PTT treatment *in vivo* and *in vitro*. The tumor model was built by hypodermic injection with 8×10^6 HeLa cells in the back of BALB/C mice. The tumor models were further cultured to reach about ~4 mm in diameter. The temperature and corresponding infrared thermal images were detected by a Ti 95 thermal IR cameral (Ti 95, Fluke, USA). The tumor size was measured everyday after the treatment through the equation[10]:

$$V= ab^2/2$$

where a and b represent the length and width of tumor, respectively.

Photothermal performance measurement. To estimate the photothermal performance, CDs-based aqueous solutions (1 mL, 15 mg/mL) were irradiated by 808 nm laser (0.7 W cm^{-2}) until reaching a steady-state temperature. A Ti 95 thermal IR camera was used to record the solution temperature. Then the photothermal conversion efficiency (η) was measured by following formula[10]:

$$\eta = \frac{hA(T_{max} - T_{surr}) - Q_{dis}}{I(1 - 10^{-A_\lambda})}$$

where h and A represent the heat transfer coefficient and surface area of the container, respectively. T_{max} and T_{surr} indicate the equilibrium temperature (47.2 ℃) and ambient temperature (25 ℃), respectively.[10] Q_{dis} denotes the heat dissipation from the quartz cell. I represents laser power (0.7 W cm^{-2}), A_λ represents the absorbance of CDs solution at wavelength of 808 nm (1.71). The hA value is calculated by the following formula[10]:

$$hA = \frac{mC_p}{\Gamma_s}$$

where m indicates the solution mass (1 g), C_p represents the heat capacity (4.2 j/(g.℃) of water. r_s is the sample time constant. We further introduced θ to get the value of r_s, and the r_s can be calculated via the following formula[10]:

$$\Gamma_s = \frac{t}{\ln \theta}$$

$$\theta = \frac{T_{amb} - T_{surr}}{T_{max} - T_{surr}}$$

where T_{amb} indicates solution temperature. Thus, the r_s is derived through the linear time data vs -Ln θ

Quantum yield measurement. The QY of CDs was determined through utilizing a NIR-II emissive IR-26 dissolved in Dichloroethane (QY=0.5%) as reference[36,41]. The QY of CDs was estimated based on the following manner [36,41]:

$$\Phi_s = \Phi_r (F_s/F_r)*(A_r/A_s)*(n^2_s/n^2_r)$$

where Φ is QY, F is NIR-II emitting intensity, A is the absorption value at 800 nm wavelength and n represents the refractive index of solvent (water: 1.33; dichloroethane:1.44).[41] The subscripts s and r indicate the CDs sample and IR-26 reference, respectively.

Measuring CDs excretion rate in urine. Kunming mice were injected 200 μL of CDs through tail vein to measure the quantitative excreted rate of CDs. The urines were gathered at different post-injection times over 24 h. We further measured the fluorescence intensity of urine by using the small animal imaging system.[41] The renal excretion rate of CDs was measured based on the previously reported method [36,41]. The injected dose (%ID) was achieved based on the following method[36,41] :

$$\%ID = \frac{\sum_{m=s_1}^{m=s_f}\left(I_m - I_{control}\right) * V_m}{\left(I_{injected} - I_{control}\right) * V_{injected}}$$

where s is the number of urine collected at different time points (S_1: the first time point, S_f: the last time point), I represents the average NIR-II signal intensity of urine, $I_{control}$ is the NIR-II signal intensity of urine taken from untreated mouse, $I_{injected}$ is the NIR-II signal intensity of injected CDs solution, V_m is the urine volume collected at different times, and $V_{injected}$ represents the injected dose of CDs solution.

Histology analysis. For further evaluation biotoxicity of CDs, histology analysis of kunming mice treated with CDs was performed. Kunming mice treated with CDs solution after 5 and 10 days and control mouse were dissected to obtain the main organs. The obtained heart, liver, spleen, lung, and kidney organs were then stained by hematoxylin and eosin for histology analysis[41].

ASSOCIATED CONTENT

AUTHOR INFORMATION

Corresponding Author

songjunz@hunnu.edu.cn, jh.hao@polyu.edu.hk

Notes

The authors declare no competing financial interest.

ACKNOWLEDGMENT

This work was supported by the National Natural Science Foundation of China (No. 21671064), Science and Technology Planning Project of Hunan Province (No. 2017RS3031).

REFERENCES

(1) Qu, S. N.; Wang, X. Y.; Lu, Q. Q.; Liu, X. Y.; Wang, L. J. A biocompatible fluorescent ink based on water-soluble luminescent carbon nanodots. *Angew. Chem., Int. Ed.* **2012**, *51*, 12381-12384.

(2) Zhu, S. J.; Meng, Q. N.; Wang, L.; Zhang, J. H.; Song, Y. B.; Jin, H.; Zhang, K.; Sun, H. C.; Wang, H. Y,; Yang, B. Highly photoluminescent carbon dots for multicolor patterning, sensors, and bioimaging. *Angew. Chem., Int. Ed.* **2013**, *52*, 4045-4049.

(3) Qu, S. N.; Zhou, D.; Li, D.; Ji, W. Y.; Jing, P. T.; Han, D.; Liu, L.; Zeng, H. B.; Shen, D. Z. Toward efficient orange emissive carbon nanodots through conjugated sp^2-domain controlling and surface charges engineering. *Adv. Mater.* **2016**, *28*, 3516-3521.

(4) Lu, S. Y.; Cong, R. D.; Zhu, S. J.; Zhao, X. H.; Liu, J. J.; Tse, J. S.; Meng, S.; Yang, B. pH-dependent synthesis of novel structure-controllable polymer-carbon nanodots with high acidophilic luminescence and super carbon dots assembly for white light-emitting diodes. *ACS Appl. Mater. Interfaces.* **2016**, *8*, 4062-4068.

(5) Ding, H.; Yu, S. B.; Wei, J. S.; Xiong, H. M. Full-color light-emitting carbon dots with a surface-state-controlled luminescence mechanism. *ACS Nano* **2016**, *10*, 484.

(6) Yang, S. T.; Cao, L.; Luo, P. G. J.; Lu, F. S.; Wang, X.; Wang, H. F.; Meziani, M. J.; Liu, Y. F.; Qi, G.; Sun, Y. P. Carbon dots for optical imaging *in vivo. J. Am. Chem. Soc.* **2009**, *131*, 11308-11309.

(7) Liu, J. J.; Lu, S. Y.; Tang, Q. L.; Zhang, K.; Yu, W. X.; Sun, H. C.; Yang, B. One-step hydrothermal synthesis of photoluminescent carbon nanodots with selective antibacterial activity against Porphyromonas. *Nanoscale*, **2017**, *9*, 7135-7142.

(8) Liu, J. J.; Li, D. W.; Zhang, K.; Yang, M. X.; Sun, H. C. and Yang, B. One-step hydrothermal synthesis of nitrogen-doped conjugated carbonized polymer dots with 31% efficient red emission for *in vivo* imaging. *Small*, **2018**, *14*, 1703919.

(9) Li, D.; Jing, P. T.; Sun, L. H.; An, Y.; Shan, X. Y.; Lu, X. H.; Zhou, D.; Han, D.; Shen, D. Z.; Zhai, Y. C.; Qu, S. N.; Zborˇil, R. and Rogach, A. L. Near-infrared excitation/emission and multiphoton-induced fluorescence of carbon dots. *Adv. Mater*. **2018**, *30*, 1705913.

(10) Ge, J. C.; Jia, Q. Y.; Liu, W. M.; G, L.; Liu, Q. Y.; Lan, M. H.; Zhang, H. Y.; Meng, X. M.; Wang, P. F. Red-emissive carbon dots for fluorescent, photoacoustic, and thermal theranostics in living mice. *Adv. Mater*. **2015**, *27*, 4169-4177.

(11) Zheng, M.; Liu, S.; Li, J.; Qu, D.; Zhao, H. F.; Guan, X. G.; Hu, X. L.; Xie, Z. G.; Jing, X. B.; Sun, Z. H. Integrating oxaliplatin with highly luminescent carbon dots: an unprecedented theranostic agent for personalized medicine. *Adv. Mater*. **2014**, 26, 3554-3560.

(12) Song, Y. B.; Zhu, S. J.; Yang, B. Bioimaging based on fluorescent carbon dots. *RSC Adv.*, **2014**, *4*, 27184-27200.

(13) Li, X. M.; Rui, M. C; Song, J. Z.; Shen, Z. H.; Zeng, H. B. Carbon and graphene quantum dots for optoelectronic and energy devices. *Adv. Funct. Mater*. **2015**, *25*, 4929.

(14) Lim, S. Y.; Shen, W.; Gao, Z.; Carbon quantum dots and their applications. *Chem. Soc. Rev.* **2015**, *44*, 362-381.

(15) Ding, C. Q.; Zhu, A. W.; Tian, Y. Functional surface engineering of C-dots for fluorescent bsensing and *in vivo* bioimaging. *Acc. Chem. Res.* **2014**, *47*, 20-30.

(16) Baker, S. N.; Baker, G. A. Luminescent carbon nanodots: emergent nanolights. *Angew. Chem.* **2010** , *122* , 6726-6744.

(17) Zhang, Z. P.; Zhang, J.; Chen, N.; Qu, L. T.; Graphene quantum dots: an emerging material for energy-related applications and beyond. *Energy. Environ. Sci.* **2012**, *5*, 8869-8890.

(18) Cao, L.; Wang, X.; Meziani, M. J.; Lu, F. S.; Wang, H. F.; Luo, P. G.; Lin, Y.; Harruff, B. A.; Veca, L. M.; Murray, D.; Xie, S.Y. and Sun, Y. P. Carbon dots for multiphoton bioimaging. *J. Am. Chem. Soc.*, **2007**, *129*, 11318-11319.

(19) Welsher, K.; Liu, Z.; Daranciang, D.; Dai, H. J. Selective probing and imaging of cells with single walled carbon nanotubes as near-infrared fluorescent molecules. *Nano Lett*. **2008**, *8*, 586-590.

(20) Hong, G. S.; Zou, Y. P.; Antaris, A. L.; Diao, S.; Wu, D.; Cheng, K.; Zhang, X. D.; Chen, X.; Liu, B.; He, Y. H.; Wu, J. Z.; Yuan, J.; Zhang, B.; Tao, Z. M.; Fukunaga, C & Dai, H. J. Ultrafast fluorescence imaging *in vivo* with conjugated polymer fluorophores in the second near-infrared window. *Nat. Commun.* **2014**, *5*, 4206.

(21) Lan, M. H.; Zhao, S. J.; Zhang, Z. Y.; Yan, L.; Guo, L.; Niu, G. L.; Zhang, J.; Zhao, J. F.; Zhang, H. Y.; Wang, P. F.; Zhu, G. Y.; Lee, C. S.; Zhang, W. Two-photon-excited near-infrared emissive carbon dots as multifunctional agents for fluorescence imaging and photothermal therapy. *Nano Res.* **2017**, *10*, 3113-3123.

(22) Luo, P. G.; Sahu, S.; Yang, S. T.; Sonkar, S. K.; Wang, J.; Wang, H.; LeCroy, G. E.; Cao, L.; Sun, Y. P. Carbon "quantum" dots for optical bioimaging. *J. Mater. Chem. B* **2013**, *1*, 2116-2127.

(23) Zhu, S.; Wang, L.; Li, B.; Song, Y.; Zhao, X.; Zhang, G.; Zhang, S.; Lu, S.; Zhang, J.; Wang, H.; Sun, H.; Yang, B. Investigation of photoluminescence mechanism of graphene quantum dots and evaluation of their assembly into polymer dots. *Carbon* **2014**, *77*, 462-472.

(24) Welsher, K.; Liu, Z.; Sherlock, S. P.; Robinson, J. T.; Chen, Z.; Daranciang, D.; Dai, H. J. A route to brightly fluorescent carbon nanotubes for near-infrared imaging in mice. *Nat. Nanotechnol.* **2009**, *4*, 773-780.

(25) Welsher, K.; Sherlock, S. P.; Dai, H. J. Deep-tissue anatomical imaging of mice using carbon nanotube fluorophores in the second near-infrared window. *Proc. Natl. Acad. Sci. USA.* **2011**, *108*, 8943-8948.

(26) Robinson, J. T.; Hong, G. S.; Liang, Y. Y.; Zhang, B.; Yaghi, O. K.; Dai, H. J. *In vivo* fluorescence imaging in the second near-infrared window with long circulating carbon nanotubes capable of ultrahigh tumor uptake. *J. Am. Chem. Soc.* **2012**, *134*, 10664-10669.

(27) Hong, G. S.; Lee, J. C.; Robinson, J. T.; Raaz, U.; Xie, L.; Huang, N. F.; Cooke, J. P. & Dai, H. J. Multifunctional *in vivo* vascular imaging using near-infrared II fluorescence. *Nat. Med.* **2012**, *18*, 1841-1846.

(28) Hong, G. S.; Diao, S.; Chang, J. L.; Antaris, A. L.; Chen, C. X.; Zhang, B.; Zhao, S.; Atochin, D. N.; Huang, P. L.; Andreasson, K. I.; Kuo, C. J.; & Dai, H. J. Through-skull fluorescence imaging of the brain in a new near-infrared window. *Nature Photonics* **2014**, *8*, 723-730.

(29) Bruns, O. T.; Bischof, T. S.; Harris, D. K.; Franke, D.; Shi, Y.; Riedemann, L.; Bartelt, A.; Jaworski, F. B.; Carr, J. A.; Rowlands, C. J.; Wilson, M. W. B.; Chen, O.; Wei, H.; Wang, G. W.; Montana, D. M.; Coropceanu, I.; Achorn, O. B.; Kloepper, J.; Heeren, J.; So, P. T. C.; Fukumura, D.; Jensen, K. F.; Jain, R. K.; Bawendi, M. G. Next-generation *in vivo* optical imaging with short-wave infrared quantum dots. *Nature Biomedical Engineering*. **2017**, *1*, 0056.

(30) Hong, G. S.; Robinson, J. T.; Zhang, Y. J.; Diao, S.; Antaris, A. L.; Wang, Q. B.; Dai, H. J. *In vivo* fluorescence imaging with Ag_2S quantum dots in the second near-infrared region. *Angew. Chem. Int. Ed*. **2012**, *51*, 9818-9821.

(31) Zhang, Y.; Hong, G.; Zhang, Y. ; Chen, G.; Li, F.; Dai, H. J.; Wang, Q. B. *In vivo* fluorescence imaging with Ag_2S quantum dots in the second near-infrared region. *ACS Nano* **2012**, *6*, 3695-3702.

(32) Rui, W.; Li, X. M.; Zhou, L.; Zhang, F. Epitaxial seeded growth of rare-earth nanocrystals with efficient 800 nm near-infrared to 1525 nm short-wavelength infrared downconversion photoluminescence for *in vivo* bioimaging. *Angew. Chem. Int. Ed.* **2014**, *53*, 1-6.

(33) Hong, G. S.; Antaris, A. L.; Dai, H. J.; Near-infrared fluorophores for biomedical imaging. *Nat. Biomed. Eng*. **2017**,*1*, 0010.

(34) Zhong, Y. T.; Ma, Z. R.; Zhu, S. J.; Yue, J. Y.; Zhang, M. X.; Antaris, A. L.; Yuan, J.; Cui, R.; Wan, H.; Zhou, Y.; Wang, W. Z.; Huang, N. G. F.; Luo, J.; Hu, Z. Y.; Dai, H. J. Boosting the down-shifting luminescence of rare-earth nanocrystals for biological imaging beyond 1500 nm. *Nat. Commun*. **2017**, *8*, 737.

(35) Chen, Y.; Montana, D. M.; Wei, H.; Cordero, J. M.; Schneider, M. X. L.; Chen, O.; Bruns, O. T.; Bawendi, M. G. Shortwave infrared *in vivo* imaging with gold nanoclusters. *Nano Letters*. **2017**, *17*, 6330-6334.

(36) Antairs, A. L.; Chen, H.; Cheng, K.; Sun, Y.; Hong, G. S.; Qu, C. R.; Qu, S.; Deng, Z. X.; Hu, X. M.; Zhang, B.; Zhang, X. D.; Yaghi, O. K.; Alamparambil, Z. R.; Hong, X. C.; Cheng, Z.; Dai, H. J. A small-molecule dye for NIR-II imaging. *Nature Materials* **2016**, *15*, 235-242.

(37) Sun, Y. P.; Zhou, B.; Lin, Y.; Wang, W.; Fernando, K. A. S.; Pathak, P.; Meziani, M. J.; Harruff, B. A.; Wang, H. F.; Luo, P. J. G.; Yang, H.; Kose, M. E.; Chen, B. L.; Veca, L. M. and Xie, S. Y. Quantum-sized carbon dots for bright and colorful photoluminescence. *J. Am. Chem. Soc.* **2006**, *128*, 7756-7757.

(38) Li, H. T.; He, H. D.; Kang, Z. H.; Huang, H.; Liu, Y.; Liu, J. L.; Lian, S. Y.; Tsang, C. H. A.; Yang, X. B.; Lee, S. T. Water‐soluble fluorescent carbon quantum dots and photocatalyst design. *Angew. Chem. Int. Ed.* **2010**, *49*, 4430-4434.

(39) Bao, L.; Liu, C.; Zhang, Z. L.; Pang, D. W. Photoluminescence-tunable carbon nanodots: surface-state energy-gap tuning. *Adv. Mater.* **2015**, *27*, 1663-1667.

(40) Bao, L.; Zhang, Z. L.; Tian, Z. Q.; Zhang, L.; Liu, C.; Lin, Y.; Qi, B. P.; Pang, D. W. Electrochemical tuning of luminescent carbon nanodots: from preparation to luminescence mechanism. *Adv. Mater.* **2011**, *23*, 5801-5806.

(41) Li, Y. B.; Li, X. L.; Xue, Z. L.; Jiang, M. Y.; Zeng, S. J.; Hao, J. H. Second near-infrared emissive lanthanide complex for fast renal-clearable *in vivo* optical bioimaging and tiny tumor detection. *Biomaterials*, **2018,** *169*, 35-44.

(42) Xue, Z. L.; Zeng, S. J.; Hao. J. H. Non-invasive through-skull brain vascular imaging and small tumor diagnosis based on NIR-II emissive lanthanide nanoprobes beyond 1500 nm. *Biomaterials*, **2018**, *171*, 153-163.

(43) Wang, J. Q.; Liu, G. Imaging nano–bio interactions in the kidney: toward a better understanding of nanoparticle clearance. *Angew. Chem. Int. Ed.* **2018**, *57*, 2-5.

(44) Chen, H. L.; Song, M. L.; Tang, J.; Hu, G. F.; Xu, S. Y.; Guo, Z. D.; Li, N. N.; Cui, J. B.; Zhang, X. Z.; Chen, X. Y.; Wang, L. Y. Ultrahigh 19F loaded $Cu_{1.75}S$ nanoprobes for simultaneous 19F magnetic resonance imaging and photothermal therapy. *ACS Nano*, **2016**, *10*, 1355-1362.

(45) Zhang, M.; Wang, J.; Wang, W. T.;Zhang, J.; Zhou, N. L. Magnetofluorescent photothermal micelles packaged with GdN@CQDs as photothermal and chemical dual-modal therapeutic agents. *Chem. Eng. J.* **2017**, 330, 442-452.

(46) Ren, X. Q.; Zheng, R.; Fang, X. L.; Wang, X. F.; Zhang, X. Y.; Yang, W. L.; Sha, X. Y. Red blood cell membrane camouflaged magnetic nanoclusters for imaging-guided photothermal therapy. *Biomaterials*,**2016**, *92*, 13-24.

(47) Wu, F.; Zhang, M.; Lu, H. W.; Liang, D.; Huang, Y. L.; Xia, Y. H.; Hu, Y. Q.; Hu, S. Q.; Wang, J. X.; Yi, X. Y. and Zhang, J. Synthesis of novel cyclodextrin-modified reduced graphene oxide composites by a simple hydrothermal method. *ACS Appl. Mater. Interfaces*, 2018, **10**, 21939–21949.

(48) Zhang, M.; Wang, W. T.; Cu, Y. J.; Zhou, N. L. and Shen, J. Magnetofluorescent carbon quantum dot decorated multiwalled carbon nanotubes for dual-modal targeted imaging in chemo-photothermal synergistic therapy. *ACS Biomater. Sci. Eng.* **2018**, *4*, 151-162.